Chapter 9
Coupled THM-Processes

Jobst Maßmann, Fabien Magri, Wenqing Wang, Elena Tiller, Thomas Kempka, Norihiro Watanabe, Günter Zimmermann, Xuerui Wang, Son Nguyen and Hua Shao

9.1 2D Axially Symmetric and 3D Simulations of THM Processes at the EBS Experiment, Horonobe URL (Japan)

Jobst Maßmann

9.1.1 Introduction

The DECOVALEX project is an international research and model comparison collaboration in the field of coupled THM simulations of processes concerning the safe geological storage of nuclear waste (DEC 2015). In the current project phase

J. Maßmann (✉) · X. Wang (✉) · H. Shao
BGR, Federal Institute for Geosciences and Natural Resources, Hannover, Germany
e-mail: Jobst.Massmann@bgr.de

X. Wang
e-mail: xuerui.Wang@bgr.de

F. Magri (✉) · W. Wang · N. Watanabe
UFZ, Helmholtz Centre for Environmental Research, Leipzig, Germany
e-mail: fabien.magri@ufz.de

E. Tiller · T. Kempka · G. Zimmermann
GFZ, Helmholtz Centre Potsdam, German Research Centre for Geosciences, Hannover, Germany

S. Nguyen
CNSC, Canadian Nuclear Safety Commission, Ottawa, Canada

O. Kolditz et al. (eds.), *Thermo-Hydro-Mechanical-Chemical Processes in Fractured Porous Media: Modelling and Benchmarking*, Terrestrial Environmental Sciences, DOI 10.1007/978-3-319-29224-3_9

"DECOVALEX2015", one of the tasks is proposed by the Japan Atomic Energy Agency (JAEA). It focuses on THM simulations for the full-scale Engineering Barrier System (EBS) experiment as a part of the Horonobe Underground Research Laboratory (URL) project in Japan (Sugita and Nakama 2012).

In the following 2D axially symmetric and 3D simulations, performed with OGS, will be presented. The main emphasis is laid on the desaturation and resaturation processes in the near field of the heater and the THM coupled effects.

9.1.2 Model Setup

The model of the EBS experiment comprises the surrounding claystone, an open drift, a plug, support and floor, backfill and buffer and the heater. The material of the plug, support and floor is concrete with the same properties. The buffer and the backfill consist of different kinds of bentonite. This model approach considers the heating phase only. The general model setup, including the initial (IC) and boundary conditions (BC), is depicted in Fig. 9.1. The material properties are listed in Table 9.1. The material properties and geometries have been provided within the DECOVALEX2015 project and are mainly based on Sugita and Nakama (2012), Sugita (2013), Sugita (2014) and JNC (2000). The initial and boundary conditions in the 2D model are set accordingly to the 3D model. As a matter of course, the open drift and the plug cannot be considered in a 2-dimensional approach. Furthermore, the shape of the backfill and concrete area are simplified in the axially symmetric model.

The hydraulic problem is described by a non-isothermal Richard's flow in a deformable porous medium considering vapour diffusion. The water retention curves are depicted in Fig. 9.2. The fluid viscosity and the fluid density are defined as non linear functions of temperature. The values for the fluid density are taken from the NIST

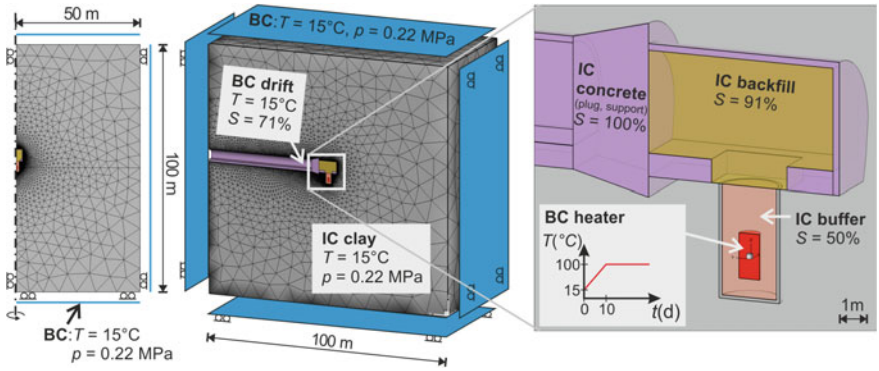

Fig. 9.1 Model setups of the 2D axially symmetric (*left*) and the 3D model (*center* and *right*)

Table 9.1 Material properties, based on Sugita and Nakama (2012), Sugita (2013), Sugita (2014) and JNC (2000)

Parameter	Clay	Buffer	Backfill	Concrete	Fluid	Unit
Particle density, ρ	2454.0	2680.0	2593.0	2621.0	$f(T)$	kg/m^3
Porosity, n	0.45	0.4	0.46	0.13	–	–
Intrinsic permeability, k	1.33e−15	1.4e−20	1.76e−19	1.0e−17	–	m^2
Young's modulus, E	1820.0	37.0	3.0	20,000.0	–	MPa
Poisson's ratio, ν	0.21	0.3	0.3	0.3	–	–
Specific heat capacity, c_p	626.0	341.0	300.6	871.7	4180.0	J/(kg·K)
Cubic th. exp. coeff., β	1.3e−5	1.0e−6	8.0e−6	1.3e−5	$f(\rho_w)$	1/K
Thermal conductivity, κ	$f(Sw)$	$f(Sw)$	1.7	2.85	0.6	W/(m·K)
Biot's coefficient, α	1.0	1.0	1.0	1.0	–	–
Max. swell. press., $p_{sw,max}$	0.0	5.0e5	8.6e5	0.0	–	–

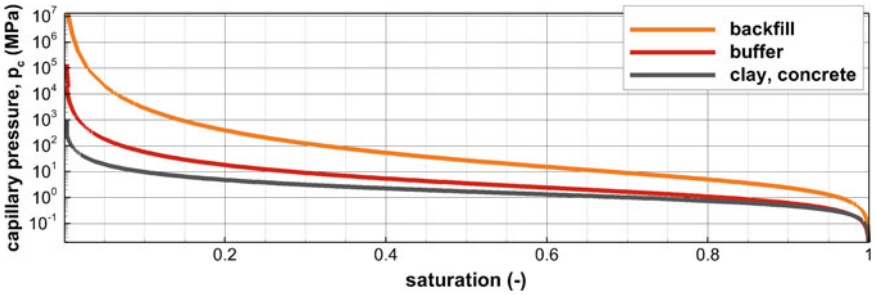

Fig. 9.2 Water retention curves for the clay and buffer (both based on Sugita (2013)) backfill (based on Sugita (2014)) and concrete

database (Lemmon et al. retrieved Oct 2014). Since the thermal expansion of the fluid is defined by the derivative of the density with respect to temperature, the thermal expansion of the fluid depends on temperature, too. The viscosity μ is calculated by a function published by Yaws et al. (1976) with the absolute temperature T_{abs}:

$$\ln \mu = -24.7 + \frac{421}{T_{abs}} + 0.0453\, T_{abs} - 0.0000338\, T_{abs}^2 \,. \tag{9.1.1}$$

The deformation behaviour is simulated by a linear elastic model taking into account thermal expansion, saturation dependent swelling/shrinkage and the pore water pressure. Thus, the conservation of linear momentum can be stated as:

$$\nabla \cdot (\boldsymbol{\sigma} - \alpha\chi p\mathbf{1} - S_w p_{sw,max}\mathbf{1} - \beta_s \mathbf{C}\Delta T) = 0\,, \tag{9.1.2}$$

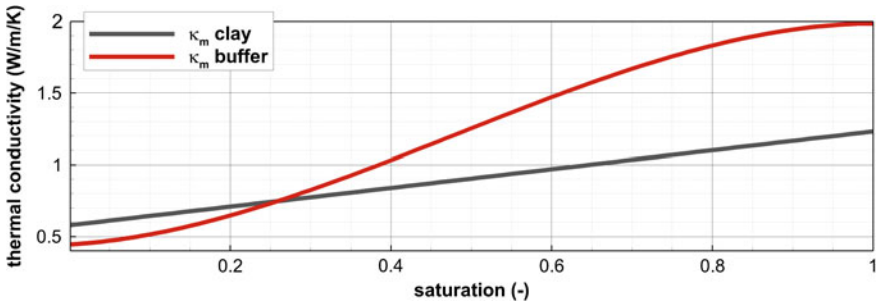

Fig. 9.3 Thermal conductivities of the porous media clay and buffer

where $\boldsymbol{\sigma}$ represents the tensor of effective stresses, α the Biot coefficient, p the pore water pressure, S_w the degree of water saturation, $p_{\mathrm{sw,max}}$ the maximum swelling stress, β_s the cubic thermal expansion coefficient of the solid phase, $\mathbf{C}$ the tensor of elasticity and T the temperature. The Bishop coefficient χ is defined as:

$$\chi = \begin{cases} 0, & \text{if } S_\mathrm{w} < 1 \\ 1, & \text{else} \end{cases} . \tag{9.1.3}$$

Consequently, in the unsaturated case the coupling between pore water pressure and total stresses by the effective stress approach is neglected and the HM coupling is modelled by the linear swelling model only.

The thermal conductivities of the porous media κ_m of the buffer and the clay are presented in Fig. 9.3. The general mixture theory is applied in the backfill and the concrete with the porosity n and the indices s and w for solid and water, respectively:

$$\kappa_\mathrm{m} = (1 - n)\kappa_\mathrm{s} + nS_\mathrm{w}\kappa_\mathrm{w} . \tag{9.1.4}$$

9.1.3 Discussion of Results

The simulated temperature and degree of water saturation are depicted in Figs. 9.4 and 9.5. A comparison between the results of the 3D model and the 2D axially symmetric model approach along a vertical line shows a good agreement. After 7 years the temperature above the heater calculated by the 2D model is slightly higher. This can be explained by the influence of the open drift in the 3D model, where a temperature boundary condition ($T = 15\,°\mathrm{C}$) acts as a heat sink. Nearby the heater, the saturation is decreased due to vapour diffusion. After 7 years, the backfill is nearly saturated but the buffer only partially.

The heating and resaturation induce a change of pore water pressure and the stress field (Fig. 9.6). The results are strongly influenced by the wide-ranging mechanical and hydraulic material properties. Some THM coupling effects can be observed: the temperature rise leads to compression, strengthened by swelling due to increase of

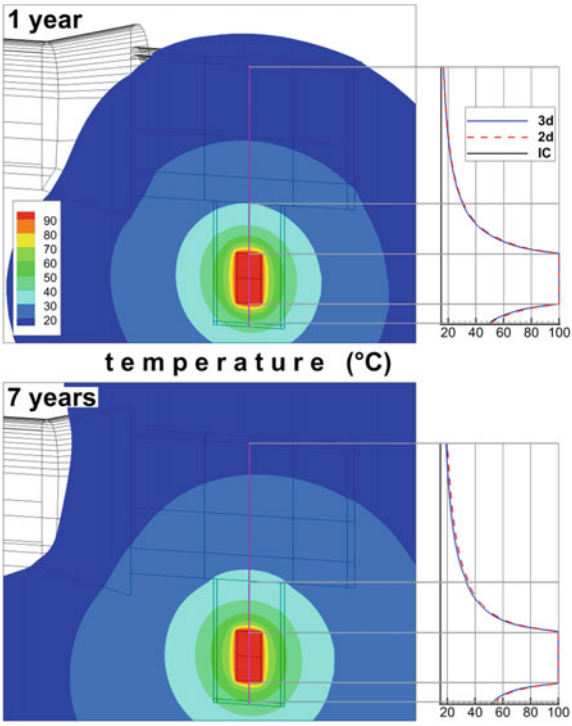

Fig. 9.4 Simulated temperature after 1 and 7 years of heating; *right*: results along a *vertical line*

saturation, and thus, negative stresses occur. This phenomena is observable in the buffer as well as in the parts of the claystone and the comparatively stiff concrete, where a noticeable increase in temperature takes place. Close to the heater, this effect is superimposed by shrinkage, due to a decrease of saturation, which leads to tensional stresses. In the upper parts of the concrete the temperature change is small and the pore water pressure increases because of the initial and boundary conditions of the rock. In these areas tensional stresses can be observed, caused by the effective stress principle.

Overall it can be stated that different THM coupling effects takes place due to heating and resaturation. In some areas, they are mutually reinforcing, in others they are mutually weakening.

Acknowledgments

The authors appreciate and thank the Funding Organisations for their financial and technical support of the DECOVALEX project work described in this paper. The statements made in the paper are, however, solely those of the authors and do not necessarily reflect those of the Funding Organisation(s). Also, no responsibility is assumed by the authors for any damage to property or persons as a result of operation or use of this publication and/or the information contained herein.

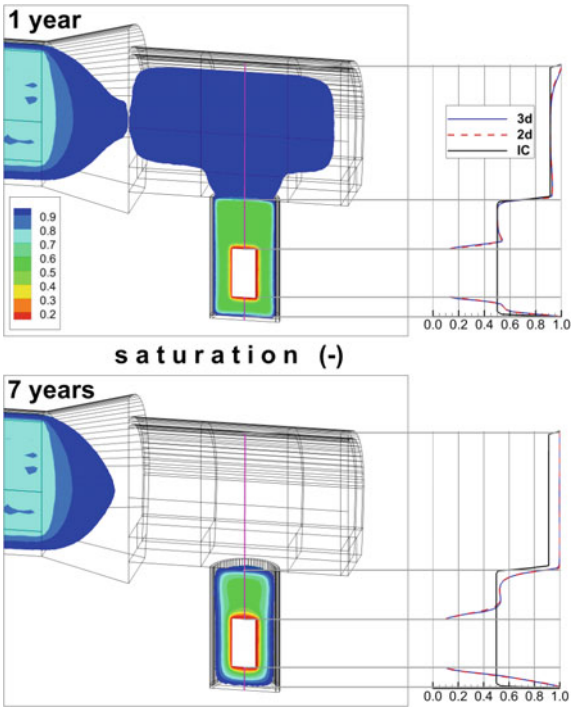

Fig. 9.5 Simulated saturation after 1 and 7 years of heating; *right*: results along a vertical line

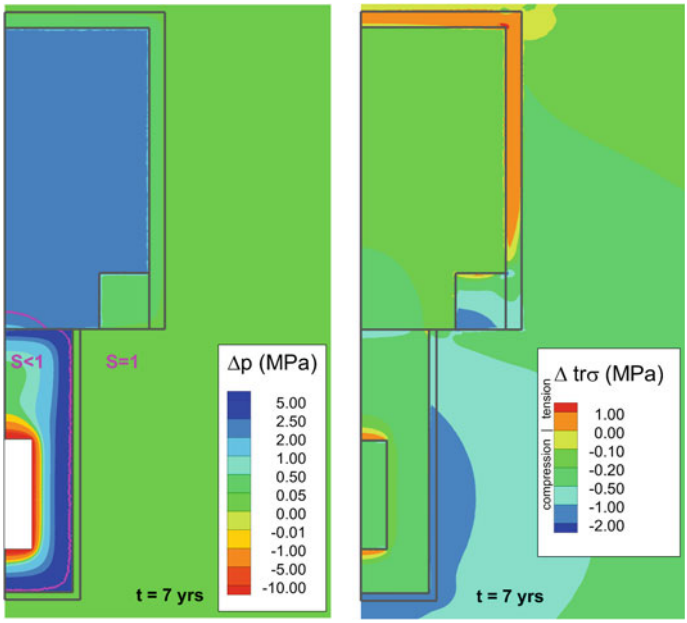

Fig. 9.6 Simulated changes in the pore water pressure and stresses due to 7 years of heating

9.2 HM/THM Processes in a Faulted Aquifer

Fabien Magri, Elena Tillner, Thomas Kempka, Norihiro Watanabe, Wenqing Wang, Günter Zimmermann

Hydro-Mechanical (HM) and transient Thermo-Hydro-Mechanical (THM) simulations in a faulted aquifer are presented. Both 2D and 3D scenarios are illustrated. OpenGeoSys (OGS) results are compared with those obtained using ABAQUS Abaqus (2007), a commercial finite element software with wide material modeling capability, including coupled hydraulic and mechanical processes in porous media. To some extent, the results comparison validates OGS numerical capabilities in solving 2D and 3D HM and THM problems.

9.2.1 Definition

The model geometry is shown in Fig. 9.7. The model is a 900 × 900 m cube including a 100 m thick storage aquifer embedded in a sedimentary fill. A 20 m wide fault with a dip angle of 80° cuts all units. The fault is conceptually modeled as an equivalent porous media, i.e. a unit made of solid elements with their own hydraulic and mechanical physical properties. Both ABAQUS and OGS numerical simulations use the same 3D mesh. For the HM case, the grid consists of 62,818 nodes and 359,566 tetrahedral elements. Elements near the fault are 10 m wide as shown in Fig. 9.8. For THM simulations instead, ABAQUS requires hexahedral elements. Here 30 m wide

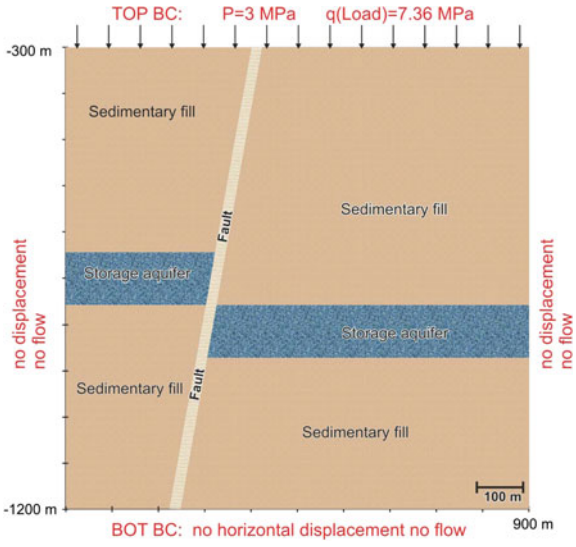

Fig. 9.7 Model geometry displaying three different units (sedimentary fill, fault and storage aquifer) and the boundary conditions of the HM problem. In the 2D simulations, the vertical profile is referred to the XY reference frame (i.e. depth in the Y direction)

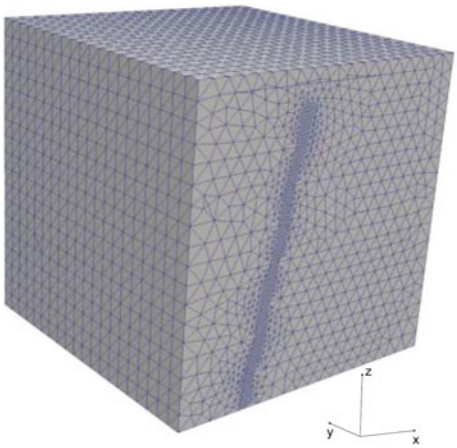

Fig. 9.8 Example of 3D finite element mesh used for HM simulations (62,818 nodes and 359,566 tetrahedral elements) in OGS and ABAQUS

first order cubes (i.e. 8 nodes) are used to discretize the sedimentary fill, whereas in the fault the resolution is still 10 m.

9.2.2 Initial and Boundary Conditions

A hydrostatic pore pressure distribution is used to initialize the simulation. For simplicity zero stress field is set over the whole model. In the paragraph "Initial conditions effects", a simulation importing a stress state as initial conditions is illustrated. Constant pore pressure (3×10^6 Pa) and stress (7.36×10^6 Pa load) are assumed as boundary conditions at the top. No flow is set on the remaining sides of the model. Null displacement conditions are applied normal to the vertical and bottom boundaries. A constant pressure of 10^8 Pa is set in the hanging wall aquifer (i.e. at the left side of the fault) in order to simulate the overpressure resulting from fluid injection. Though 10^8 Pa is not a realistic value it allows to test the software capabilities with regard to extreme pressures in a heterogeneous system.

9.2.3 Material Properties

Hydraulic and mechanical properties are given in Tables 9.2, 9.3 and 9.4, where each unit is considered isotropic and homogeneous. The fluid properties are: viscosity = 1×10^{-3} Pa s, density = 998 kg m^{-3}. Properties of the sedimentary fill and the storage aquifer represent sandstones according to data from the book by Jaeger et al. (2007).

Table 9.2 Material properties of sedimentary fill

Property	Value	Unit
Density	2500	kg/m^3
Young's modulus	2.964×10^{10}	N/m^2
Poisson's ratio	0.12	–
Permeability	2×10^{-16}	m^2
Storage coefficient	8.63×10^{-11}	Pa^{-1}
Porosity	0.04	–

Table 9.3 Material properties of storage aquifer

Property	Value	Unit
Density	2200	kg/m^3
Young's modulus	1.44×10^{10}	N/m^2
Poisson's ratio	0.20	–
Permeability	1.5×10^{-13}	m^2
Storage coefficient	8.36×10^{-11}	Pa^{-1}
Porosity	0.19	–

Table 9.4 Material properties of fault

Property	Value	Unit
Density	2200	kg/m^3
Young's modulus	1.44×10^{10}	N/m^2
Poisson's ratio	0.20	–
Permeability	1.5×10^{-12}	m^2
Storage coefficient	1.96×10^{-10}	Pa^{-1}
Porosity	0.19	–

9.2.4 Results

The calculated 2D steady state pressure, pore fluid velocity, displacement and stress fields are illustrated and directly compared with the results obtained with ABAQUS in the following.

A pressure buildup induced by the highly pressurized hanging aquifer (Fig. 9.9) develops within the fault owing to its higher hydraulic permeability (Table 9.4). Consequently, the fault acts as a preferential pathway for groundwater flow (Fig. 9.10). Deep seated fluids can flow therein at velocities ranging between 4×10^{-6} ms^{-1} to 1.4×10^{-5} ms^{-1} (i.e. 0.3 to 1.2 $mday^{-1}$), the peak velocities being observed at the boundary between the storage aquifer and the fault zone. Owing to the no displacement conditions at the lateral and bottom boundaries, major structural deformations are observed within the sedimentary fill above the hanging storage aquifer (Fig. 9.11). The calculated uplift of the surface is 2.58 m, in good agreement with ABAQUS calculations. The sliding of the hanging wall occurs along the fault plane

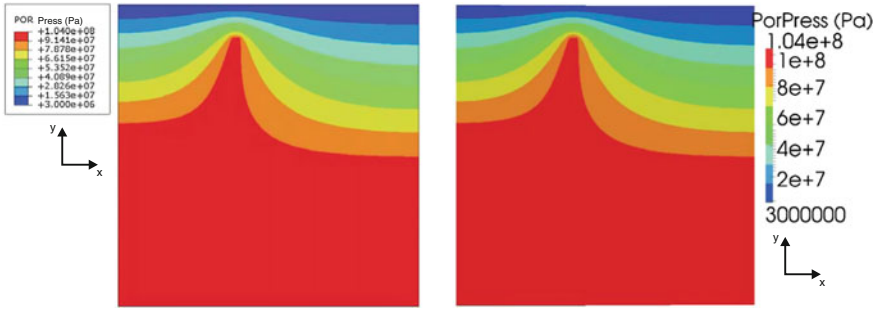

Fig. 9.9 Pore pressure (Pa) distribution calculated with ABAQUS (*left*) and OGS (*right*)

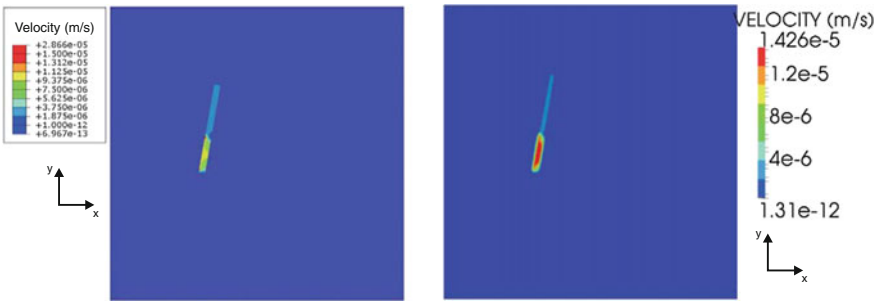

Fig. 9.10 Pore fluid velocity (ms^{-1}) calculated with ABAQUS (*left*) and OGS (*right*). Please note the different scales

Fig. 9.11 Displacement in the y direction (m) calculated with ABAQUS (*left*) and OGS (*right*)

because of the differences in the material properties between the sedimentary fill and fault, in particular the density and the elastic properties.The physical properties contrast between the fault and surrounding sediments are also reflected in the calculated stress (Fig. 9.12). In general, the stress should increase roughly linear with depth due to the increase of lithostatic pressure with depth. Here, this trend is intensely perturbed by the fault. Jumps in stress magnitude at both the top and bottom interface

Fig. 9.12 Y component of the stress field (Pa) calculated ABAQUS (*left*) and OGS (*right*)

of the fault may reach maximum values of several hundreds of MPa. Abrupt changes in stress magnitude also occur along the fault sides, as therein the stress reaches its minimal values.

9.2.5 *Initial Conditions Effects*

Here the stress and hydraulic pressure calculated with the previously described simulation are used as IC to verify whether or not the system is at hydro-mechanical equilibrium. If the mechanical equilibrium between the applied boundary conditions and the state of stress in the units has been reached, no displacement should be observed in this test case.

As a first test, a simulation is initialized with stress and hydraulic pressure fields that were calculated a priori with a two time-steps simulation. The vertical displacement is illustrated in Fig. 9.13. It can be seen that a vertical displacement exists though in the order of few millimeter (Fig. 9.13), suggesting that the stress field calculated with two time-steps is very close to mechanical equilibrium. An additional simulation initialized with stress and hydraulic pressure fields calculated with three iterations display no vertical displacement (i.e. 0 m everywhere).

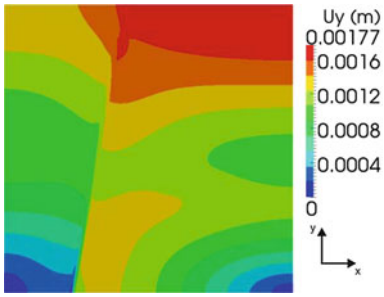

Fig. 9.13 Initial conditions effects: Displacement in the y direction (m) calculated using initial stress and hydraulic pressure fields. The IC were derived a priori with a two time-steps simulation

Table 9.5 Thermal properties of the solid and fluid used to simulate 2D and 3D THM problem

Layers	Specific heat capacity ($J\,kg^{-1}\,K^{-1}$)	Thermal conductivity ($Wm^{-1}\,K^{-1}$)	Thermal expansion coefficient (K^{-1})
Solid	900	0.6	10^{-5}
Fluid	4280	3	–

9.2.6 Temperature Effects THM Simulation

Here the results obtained from a transient Thermo–Hydro–Mechanical (THM) simulation are illustrated. Flow and mechanical boundary conditions are those pictured in Fig. 9.7. Additionally, a constant temperature of 17 °C and 44 °C are set at the top and bottom boundaries, respectively, leading to a thermal gradient of 30 K/km. For simplicity, the whole model is homogeneous with respect to thermal properties (Table 9.5). The simulation is conducted for 7.4×10^7 s (856 days) with a time step size of varying between 10^5 and 10^6 s (1–10 days). To ensure higher flow motion, the porosity of the sedimentary fill and fault are increased to 0.2 and 0.43 respectively. The other physical properties are those given in Tables 9.2, 9.3 and 9.4.

Results of temperature The hanging aquifer is saturated with fluid at 30 °C approximately. Driven by the imposed pressure gradient, groundwater flows from the storage aquifer to the fault. As a result, fluid moving upward (downward) increases (decreases) the temperature within the fold, as illustrated by convex (concave) isotherms in Fig. 9.14.

3D Results

The same set of simulations has been run for the 3D cases. OGS results well compare to those obtained with ABAQUS which validates OGS capabilities in solving 3D pressure induced stress field (Figs. 9.15, 9.16, 9.17 and 9.18).

Fig. 9.14 Temperature (°C) calculated with ABAQUS (*left*) and OGS (*right*). Temperature increase (decrease) can be observed in the fold as a result of fluid outflow from the storage aquifer into the fault

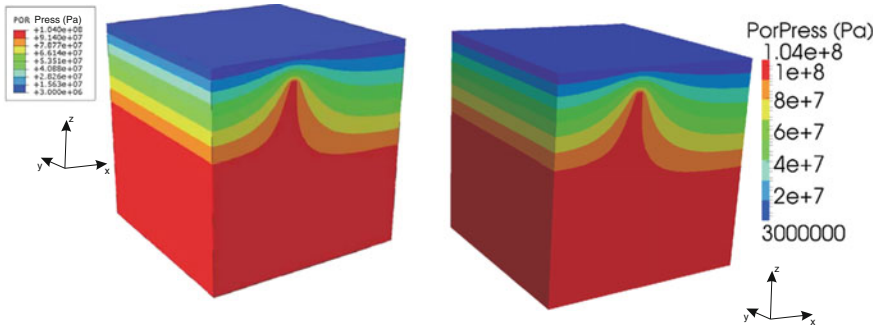

Fig. 9.15 Pore pressure (Pa) distribution calculated with ABAQUS (*left*) and OGS (*right*)

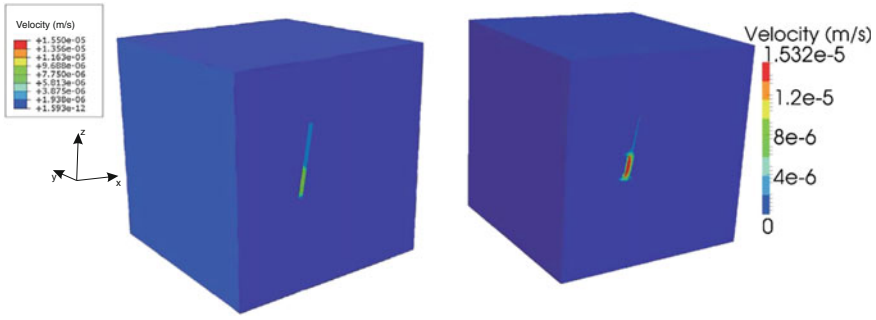

Fig. 9.16 Pore fluid velocity (m/s) calculated with ABAQUS (*left*) and OGS (*right*)

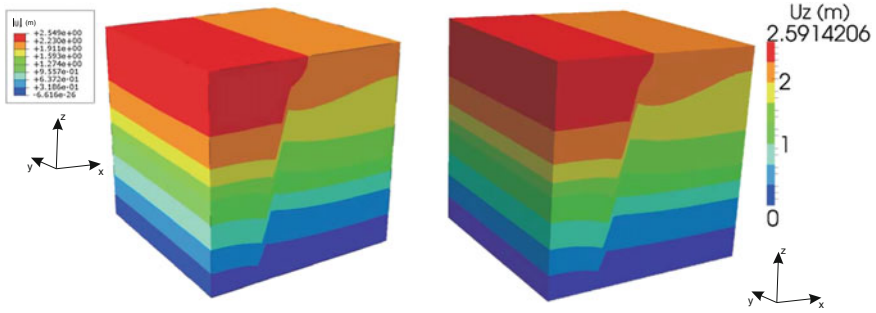

Fig. 9.17 Displacement (m) calculated with ABAQUS (*left*) and OGS (*right*)

OGS and ABAQUS results are compared at an observation point (located with the star in Fig. 9.19) for the simulated period. The temporal trends of vertical displacement (U_z) and temperature (T) are illustrated in Fig. 9.20. It can be seen that whereas the vertical displacements calculated with both software match within the error allowance, heat transport in OGS is more vigorous. The observed differences can be explained as follow: In ABAQUS, the elastic part of the volumetric behavior

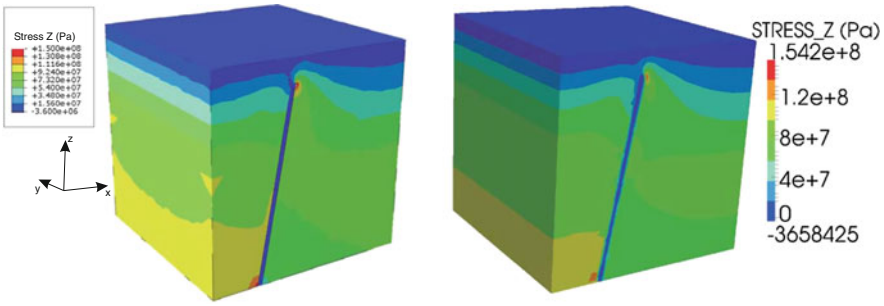

Fig. 9.18 Z component of the stress field (Pa) calculated with ABAQUS (*left*) and OGS (*right*)

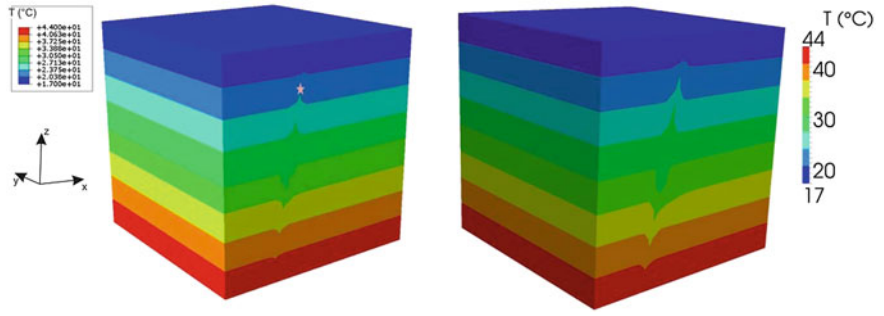

Fig. 9.19 Temperature (°C) calculated at 3×10^7 s with ABAQUS (*left*) and OGS (*right*). The star locates the observation point for the comparative graphs in Figs. 9.20 and 9.21

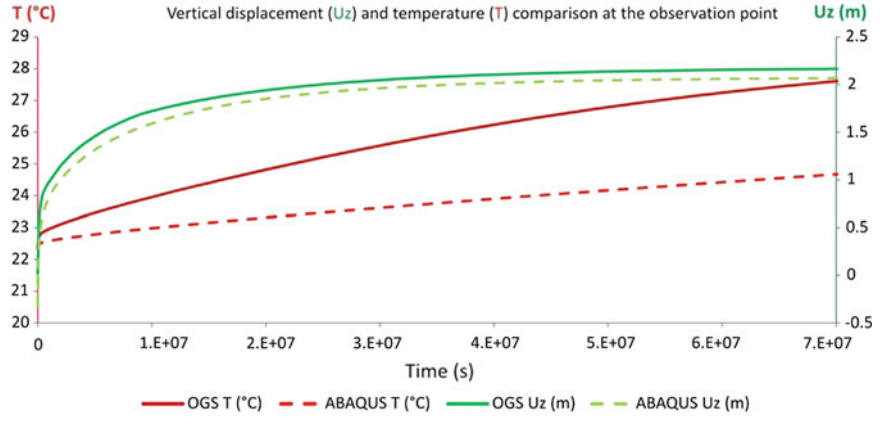

Fig. 9.20 OGS and ABAQUS comparison: Temporal trends at the observation point of the temperature (T, in °C *left* axis) and vertical displacement (U_z, in m, *right* axis)

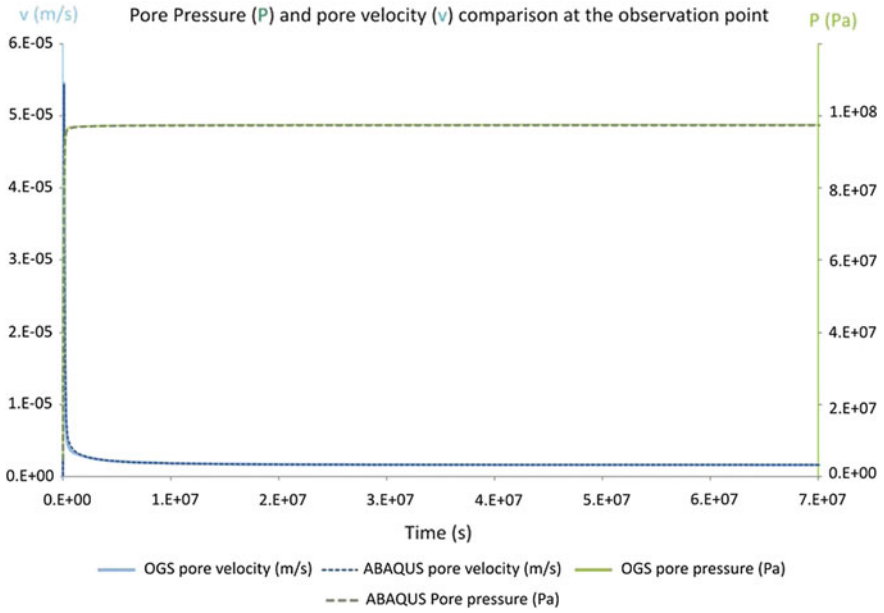

Fig. 9.21 OGS and ABAQUS comparison: Temporal trends pore velocity (v in m/s *left* axis) and pressure (P, in Pa, *right* axis), at the observation point in Fig. 9.19

is proportional to the logarithm of the pressure stress (Chap 19.3.1. ABAQUS User's manual Abaqus (2007)) whereas in OGS we assume that the elastic modulus are constant. Therefore the important fluid pressure modeled here will induce slightly different stress and displacements. In ABAQUS porosity is strain dependent. In this problem, the calculated strain increases porosity in the fold as flow evolves. Increasing porosity values lead to higher heat storage which in turn slows down heat flow. By contrast, in OGS, porosity is constant during all the simulation. OGS and ABAQUS pore pressure and pore velocity perfectly fit (Fig. 9.21). Additionally, results are provided for an observation point located inside the model at the (x, y, z) coordinates (343, −540, −400) m (Fig. 9.22).

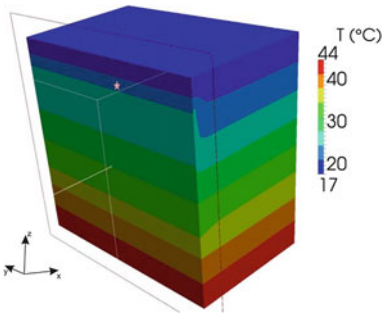

Fig. 9.22 Temperature (°C) calculated at 3×10^7 s with: OGS. The star locates the observation point for the comparative graphs in Figs. 9.23 and 9.24

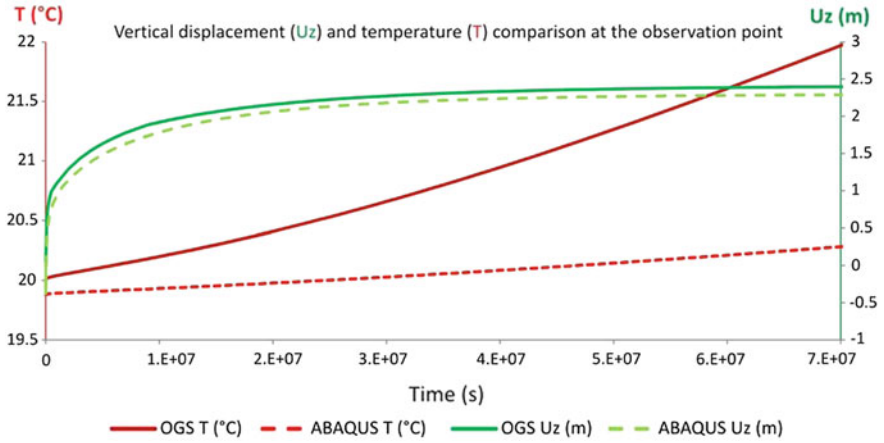

Fig. 9.23 OGS and ABAQUS comparison: Temporal trends of pore velocity (v in m/s *left* axis) and pressure (P, in Pa *right* axis) at the observation point in Fig. 9.22

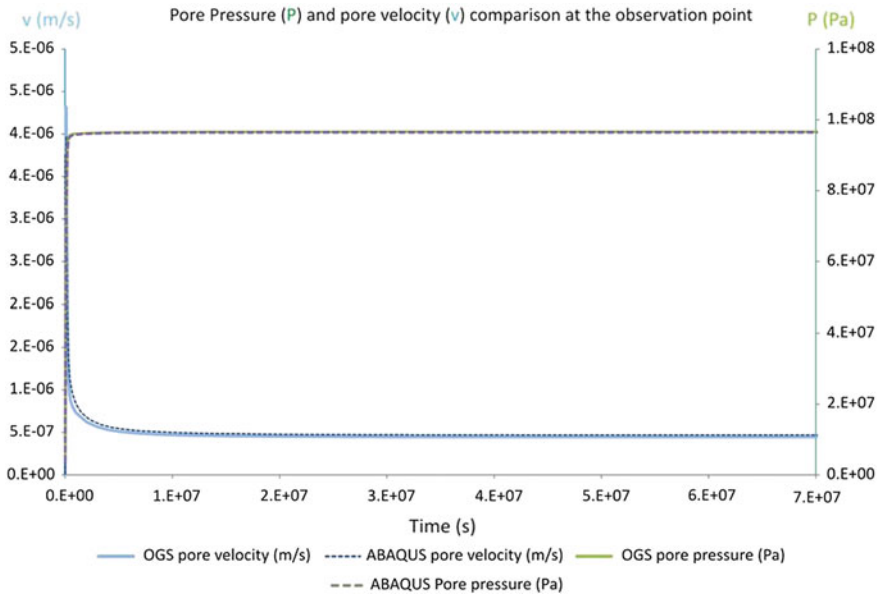

Fig. 9.24 OGS and ABAQUS comparison: Temporal trends of the temperature (T, in °C *left* axis) and *vertical* displacement (U_z, in m *right* axis) at the internal observation point in Fig. 9.22

9.3 Consolidation Around a Point Heat Source

Xuerui Wang, Son Nguyen, Hua Shao and Wenqing Wang

When a saturated porous medium is subjected to heating, a series of thermo-hydraulic-mechanical (THM) interactions will be generated. The temperature rise will lead to the expansion of pore water and solid skeleton, which will cause the increase of the pore pressure. The increase of pore pressure can then cause reduction of effective stress. If the porous medium is sufficient permeable, consolidation will occur and the excess pore pressure will dissipate.

9.3.1 Governing Equations

The equations governing the non-isothermal consolidation of a saturated porous media are:

$$c\rho\frac{\partial T}{\partial t} + c\rho\mathbf{v}\cdot\nabla T - \nabla\cdot(K\nabla T) = Q \tag{9.3.1}$$

$$G\nabla^2 u_i + (\lambda + G)\frac{\partial \varepsilon_i}{\partial x_i} + \alpha\frac{\partial p}{\partial x_i} - \beta K_D\frac{\partial T}{\partial x_i} + F_i = 0 \tag{9.3.2}$$

$$\left(\frac{n}{K_f} + \frac{a-n}{K_s}\right)\frac{\partial p}{\partial t} + \nabla\left(\frac{k_{ij}}{\mu}(\nabla p - \rho_f \mathbf{g})\right) + \frac{\partial}{\partial t}\frac{\partial u_i}{\partial x_i} - \left((1-a)\beta_u - (1-n)\beta_s - n\beta_f\right)\frac{\partial T}{\partial t} = 0 \tag{9.3.3}$$

where temperature T, pore pressure p and displacement u_i are chosen as the primary variables. c is the specific heat capacity; ρ and ρ_f are the density of bulk medium and of fluid respectively; $\mathbf{v}$ is the advection velocity; K is the thermal conductivity of porous medium; Q is the external thermal source; λ, G are the Lamé constants of the soil skeleton; K_D , K_s , K_f are the bulk moduli of drained material, solid, fluid respectively. $\alpha = 1 - K_D/K_s$ is the Biot-coefficient; F is the volumetric body force; n is porosity; β_s and β_f are the coefficients of volume expansion of soil grain and water respectively; β_s is the coefficient of volume expansion of soil. It is assumed that no structural changes occur, then $\beta_u = \beta_s$; $\mathbf{k}$ is the permeability tensor; μ is viscosity and $\mathbf{g}$ is the gravity vector.

Problem definition: We consider a point heat source of constant heat input which is located in the centre of an infinite saturated and homogenous porous medium.

9.3.2 Analytical Solution

An analytical solution for consolidation of an infinite homogenous saturated porous medium around a constant point heat source Q [W] was provided by Booker and Savvidou (1985a). The temperature, pore pressure, displacement and stress can be given by:

$$T = \frac{Q}{4\pi K R} f(\frac{\kappa t}{R^2}) \tag{9.3.4}$$

$$p = \frac{X}{1 - c_v/\kappa} \frac{Q}{4\pi K R} \left(f(\frac{\kappa t}{R^2}) - f(\frac{ct}{R^2}) \right) \tag{9.3.5}$$

$$u_i = a_u i \frac{Q}{4\pi K R} g* \tag{9.3.6}$$

$$\sigma_{ii} = 2Ga_u \frac{Q}{4\pi K R} \left(f* - g* + \frac{i^2}{R^2}(3f* - g*) \right) \tag{9.3.7}$$

$$\sigma_{ij} = 2Ga - u \frac{Q}{4\pi K R} \frac{ij}{R^2}(3f* - g*) \tag{9.3.8}$$

where κ is given by:

$$\kappa = \frac{K}{\rho c} \tag{9.3.9}$$

$$c_v = k_f(\lambda + 2G)/\gamma_w \quad \text{is the coefficient of consolidation} \tag{9.3.10}$$

$$a_u = \beta_s(1 - n) + \beta_w n \tag{9.3.11}$$

K_f is the hydraulic conductivity, γ_w is the specific weight of pore water. And

$$R = \left((x - x_s)^2 + (y - y_s)^2 + (z - z_s)^2 \right) \tag{9.3.12}$$

$$f(\frac{\kappa t}{R^2}) = \text{erfc}(\frac{R}{2\sqrt{\kappa t}}) \tag{9.3.13}$$

$$g(\frac{\kappa t}{R^2}) = \frac{\kappa t}{R^2} + (\frac{1}{2} - \frac{\kappa t}{R^2})\text{erfc}(\frac{R}{2\sqrt{\kappa t}}) - \sqrt{\frac{\kappa t}{\pi R^2}}\exp^{-R^2/4\kappa t} \quad (9.3.14)$$

where

$$f* = Yf(\frac{\kappa t}{R^2}) - Zf(\frac{ct}{R^2}) \quad (9.3.15)$$

$$g* = Yg(\frac{\kappa t}{R^2}) - Zg(\frac{ct}{R^2}) \quad (9.3.16)$$

$$X = \left(\beta_s(1-n) + \beta_f n\right)(\lambda + 2G) - (\lambda + 2G/3)\beta_u \quad (9.3.17)$$

$$Y = \frac{1}{\lambda + 2G}\left(\frac{X}{(1 - c_v/\kappa)a_u} + \frac{b'}{a_u}\right) \quad (9.3.18)$$

$$Z = \frac{1}{\lambda + 2G}\left(\frac{X}{(1 - c_v/\kappa)a_u}\right) \quad (9.3.19)$$

$i, j = x, y, z(i \neq j) and x_s, y_s, z_s$ are the coordinates of the point heat source and

$$b' = \left(\lambda + \frac{2G}{3}\right)\beta_u \quad (9.3.20)$$

9.3.3 Numerical Solution

A 3D eighth-model has been generated to analyse the aforementioned THM processes. The model domain and the boundary conditions are showed in Fig. 9.25. Symmetric conditions are specified in the model. This 3D model has a geometry of 10 m × 10 m × 10 m. The point heat source is located at the coordinate of (0, 0, 0) with the constant heat output of 300/8 W. The initial temperature and pore pressure are set as 0 °C and 0 Pa respectively. The model parameters are listed in Table 9.6. Homogenous and isotropic material properties were applied in the model. Pore water and solid are assumed as incompressible.

For the THM coupling, solid and fluid equations are solved in a monolithic manner. And the thermal equation is solved separately and iteratively with solid and fluid matrix.

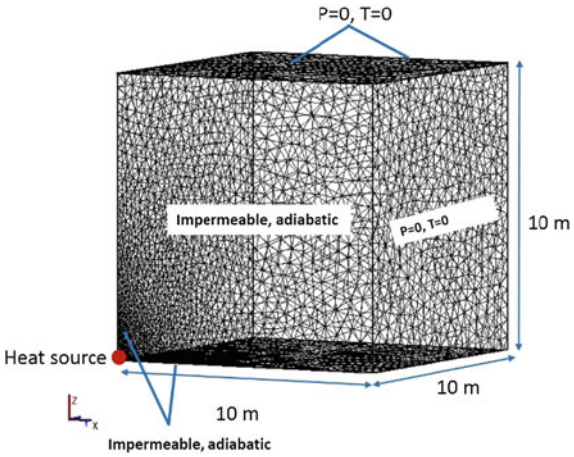

Fig. 9.25 3D model for consolidation around a point heat source

Table 9.6 Model parameters

Property	Symbol	Unit	Value
Bulk density	ρ	kg/m^3	2450
Young's modulus	E	GPa	5
Poisson ratio	ν	–	0.3
Biot coefficient	α	–	1
Thermal conductivity	K	W/m/K^{-1}	1.64
Specific heat capacity	c	J/kg/K^{-1}	1000
Porosity	n	–	0.16
Permeability	$\mathbf{k}$	m^2	2x10^{-20}
Volumetric thermal expansion coefficient			
Pore water	β_w	K^{-1}	4x10^{-4}
Solid grain	β_s	K^{-1}	4.5x10^{-5}
Porous medium	β_u	K^{-1}	4.5x10^{-5}

9.3.4 Results

In Fig. 9.26 the evolution of temperature (left) and pore pressure (right) at three points are depicted. All points are along the Z-axis and have a distance of 0.25 m (node 1), 0.5 m (node 2) and 1 m (node3) to the heat point. The calculated temperature by OGS shows a very accurate agreement with the analytical solution as well as with the calculated temperature by COMSOL. At the early stage, the pore pressure increase caused by the thermal expansion of solid and water can be numerically exactly simulated. After that consolidation occurred, during which the excess pore pressure dissipated successively. All the results show the consistence tendency. There is only slight difference among each result.

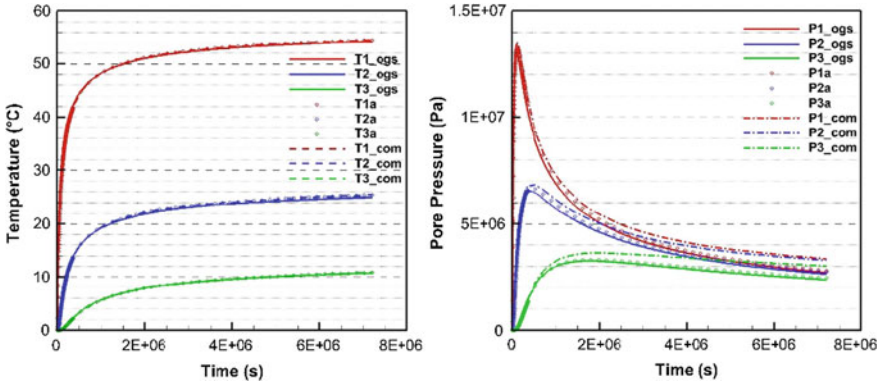

Fig. 9.26 Temperature (*left*) and pore pressure (*right*) evolutions at three different points. Comparison of the results calculated by code OGS with those of COMSOL and the analytical solution

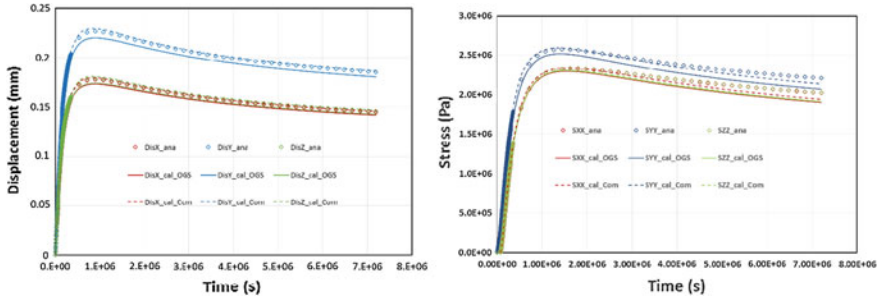

Fig. 9.27 Displacement (*left*) and stress (*right*) evolutions in X-, Y-, Z-direction at the select point. Comparison of the results calculated by code OGS with those of COMSOL and the analytical solution

Besides, one additional point of coordinate (0.4, 0.5, 0.4) outside the symmetrical axis was selected to present the mechanical results (Fig. 9.27). This point has a distance of about 0.75 m to the heat point. A fair good agreement has been achieved between the calculated results and the analytical solution. The thermal induced strain and the change of pore pressure caused firstly tensile stress in all the direction and also displacement in direction away from the heat point. After that consolidation occurred resulted in the dissipation of pore pressure, reduce of the displacement and reduce of the tensile stress.